1   **EVOLUTION OF FLOW CELLS WITHIN A MASS-TRANSPORT COMPLEX: INSIGHTS FROM**

2   **THE GORGON SLIDE, OFFSHORE NW AUSTRALIA**

3   HARYA D. NUGRAHA[1,2*], CHRISTOPHER A-L. JACKSON[1], HOWARD D. JOHNSON[1], and

4   DAVID M. HODGSON[3]

5   *[1]Basins Research Group (BRG), Imperial College, London SW7 2BP, UK*

6   *[2]Department of Geological Engineering, Universitas Pertamina, Jakarta 12220, Indonesia*

7   *[3]Stratigraphy Group, University of Leeds, Leeds LS2 9JT, UK*

8   *email: harya.nugraha14@imperial.ac.uk*

9   Keywords: submarine landslide, mass-transport complex, seismic reflection, intra-flow shear, flow

10   cells

11   **ABSTRACT**

12   Mass flows evolve longitudinally during emplacement, but can also vary laterally by forming discrete

13   flow cells with different rheological states separated by shear zones. Despite being documented in

14   many field and subsurface studies, the initiation, translation, and cessation of the flow cells remain

15   unclear. We use five, high-quality post-stack time-migrated (PSTM) 3D seismic reflection datasets to

16   investigate the evolution of flow cells in a seabed mass transport complex (MTC), the Gorgon Slide, on

17   the Exmouth Plateau, offshore NW Australia. The slide originated from a 30 km-wide, NE-SW trending

18   headwall scarp that dips steeply (*c.* 30º) seaward, and was translated to the NW over a basal-shear

19   surface that deepens downslope (up to 500 m below seafloor). The slide is dominated by chaotic

20   seismic facies with discrete packages of coherent reflectors, which is interpreted as a debrite that

21   carried megaclasts (*c.* 0.05-1 km-long) derived from the headwall domain. The morphology and

22   orientation of the basal-shear surface focused the pathway of the slide, resulting in clustering of

23   megaclasts in proximal parts of the translation domain. The megaclasts cluster became an obstacle to

24   flow, which resulted in the formation of two flow cells (Cells A and B) separated by a longitudinal shear

25   zone. The interaction between the two cells is recorded by sinuous shear bands within, and ridges on

26   the top surface of, the slide. Along the longitudinal shear zone, the shear bands and ridges of Cell A

27   were dragged downslope, due to Cell A impeding the movement of Cell B. This interaction suggests

28   that Cell B travelled faster, and/or further, than Cell A, due to the absence of any flow obstacles. The

29   abrupt cessation of Cell A is recorded by positive seabed relief, whose amplitude decreases updip. The

30   transport processes of the Gorgon Slide show how entrainment and abrasion of megaclasts induced

31   velocity perturbations during emplacement causing: (i) changes to the flow rheology, and (ii) initiation

32   and cessation of flow cells. A better understanding of how flow cells evolve during MTCs transport

33   may help to refine modelling of the potential impact of MTCs on submarine structures (e.g. pipelines,

34   cables, etc.).

35   **INTRODUCTION**

36   The degradation of submarine slopes drives emplacement of large mass-transport complexes (MTCs),

37   which are deposits of gravity-driven depositional processes that include slides, slumps and debris

38   flows (e.g. Dott 1963; Nardin et al. 1979; Nemec 1991; Moscardelli and Wood 2008; Posamentier and

39   Martinsen 2011). Besides their role in continental margin evolution (e.g. Gamboa et al. 2010) and

40   petroleum system development (e.g. Weimer and Shipp 2004), MTCs also pose a significant geohazard

41   for coastal and offshore engineering structures (e.g. Parker et al. 2008; Randolph and White 2012;

42   Vanneste et al. 2013). Understanding the magnitude of this geohazard is essential and partly depends

43   on the emplacement processes of the MTCs (Masson et al. 2006). For example, the rheology of MTCs

44   can evolve during transport (Iverson 1997; Dykstra et al. 2011; Joanne et al. 2013; Ortiz-Karpf et al.

45   2017; Hodgson et al. 2018), which controls the amount of drag forces experienced by submarine

46   pipelines (e.g. Zakeri 2009).

47   Transport processes of an MTC are dynamic, where a large, single (first-order) flow cell can evolve

48   during its translation by (i) dilution through water ingestion (Fisher 1983; Talling et al. 2012; Sun et al.

49   2018); and/or (ii) formation of smaller, second-order (intra-MTC) flow cells due to internal velocity

50 variations (Alsop and Marco 2014). In contrast to flow transformation, the formation processes of flow

51 cells remain poorly documented. Although the nature of flow cells have been inferred from outcrop

52 studies (Farrell 1984; Alsop and Marco 2014), limited outcrop extent invariably hampers full 3D

53 analysis. Studies involving 3D seismic reflection data have also documented the presence of intra-MTC

54 flow cells (Gee et al. 2005; Bull et al. 2009; Steventon et al. 2019). However, the mechanisms

55 responsible for the initiation, translation, and cessation of these flow cells remain poorly understood.

56 This work demonstrates that individual cells move at different speeds and/or at different times, as

57 indicated by flow fabrics and longitudinal shears within, and on the top surface of, MTCs (*sensu* Bull

58 et al. 2009).

59 Here, we study a recent MTC, the Gorgon Slide (hereafter the 'slide') that contains flow cells (Fig. 1).

60 We use five, high-quality 3D seismic reflection datasets from the Exmouth Plateau, offshore NW

61 Australia (Figs. 1B-C). The 3D seismic reflection datasets cover most of the Gorgon Slide area, including

62 evacuation and deposition zones, which enable us to characterise the slide from its head to toe (Fig.

63 1C). As the slide is at, or just below, the seabed, detailed seismic attribute analysis allows us to: (i)

64 document kinematic indicators on basal-shear and top surfaces, and within internal body, of the slide;

65 (ii) reconstruct emplacement processes of the slide whose kinematic indicators serve as evidence of

66 flow cells; (iii) infer the impact of flow cells on flow behaviour; (iv) discuss potential factors controlling

67 the formation of the flow cells.

68   **DATA AND METHODOLOGY**

69 We use five, high-quality post-stack time-migrated (PSTM) 3D seismic reflection datasets that image

70 the evacuation and most of the deposition zones of the Gorgon Slide (Figs. 1B-C). Only a small part of

71 the slide (7%, i.e. 166 km^2 of 1760 km^2 total area) is not imaged by the 3D seismic reflection data.

72 Thus, three 2D seismic reflection lines were used to infer the downdip limit of the deposition zone

73 (green lines in Fig. 1C). The vertical resolution of the 3D seismic reflection data at the base of the slide

74 (*c.* 500 mbsf) ranges from 8-11 m, based on near seabed sediment velocity and dominant frequency

75 of 1824 m/s and 40-60 Hz, respectively. Bin spacing of the 3D seismic volumes ranges from 12.5 x

76 18.75 m to 20 x 25 m (see Appendix 1 for details). Depth conversion of seabed and basal-shear surface

77 time structure maps was conducted by using average velocities of water (1519 m/s) and near seabed

78 sediment (1824 m/s), respectively (Appendix 1). The average water velocity is constrained by ten

79 industry wells (Fig. 1B), and the near seabed sediment velocity data is available from well ODP 762

80 (see Figs. 1A and 2).

81 The seabed and basal-shear surface of the Gorgon Slide were mapped to gain insights on the

82 kinematics of the slide during transport. We also employed an iso-proportional slicing method (Zeng

83 et al. 1998), midway between the seabed and basal-shear surface of the slide, to visualise

84 heterogeneity of internal seismic facies. Several seismic attributes were used in this analysis,

85 particularly: (i) *variance* to better image discontinuities (Chopra and Marfurt 2007), including grooves

86 on the basal-shear surface of an MTC (e.g. Bull et al. 2009); (ii) *RMS Amplitude* to better delineate

87 features that have distinct positive or negative amplitudes resulting from an acoustic (velocity and

88 density) contrast (Brown 2011), such as megaclasts encased within transparent debrite (e.g. Ortiz-

89 Karpf et al. 2017); (iii) *dip* to better image rugosity of a surface (Brown 2011), including seabed relief

90 (e.g. Bull et al. 2009); and (iv) *spectral decomposition* of seismic reflection volume was used to

91 highlight internal heterogeneities of a geological body (Partyka et al. 1999; Eckersley et al. 2018).

92   **GEOLOGICAL SETTING**

93 The Exmouth Plateau is a part of North Carnarvon Basin (NCB), a basin that experienced multiple rifting

94 events (Fig. 2) (Tindale et al. 1998; Longley et al. 2002). Deposition during the subsequent thermal

95 subsidence phase since the Cretaceous was initially dominated by fine-grained siliciclastic sediments,

96 and become carbonate-dominated as the Australian plate drifted northward towards the equator (e.g.

97 Apthorpe 1988; Hull and Griffiths 2002). Progradation of carbonate-dominated clinoforms has

98   persisted from the Oligocene to the present-day (Fig. 2B) (Cathro et al. 2003; Moss et al. 2004). A

99   collision between the Australian and Eurasian plates (Miocene to present-day) has reactivated

100   optimally oriented, pre-existing rift-related faults, forming inversion structures such as the NE-SW

101   trending Exmouth Plateau Arch (Fig. 2) (Keep et al. 1998). Emplacement of MTCs is widespread across

102   the plateau, especially during this inversion period (Boyd et al. 1993; Hengesh et al. 2013; Scarselli et

103   al. 2013), although pelagic carbonate sediments presently dominate the stratigraphy with

104   sedimentation rates as low as 20 m/Ma (Golovchenko et al. 1992). We focus on the Gorgon Slide,

105   which extends from the seabed (blue) down to its basal-shear surface (yellow, see Fig. 2B). Beneath

106   the headwall of the Gorgon Slide, there is a rift-related horst block, which was drilled by Bluebell-1

107   (Fig. 2B) (McCormack and McClay 2013). This horst contains the giant Gorgon gas field, containing 11

108   tcf of gas in place (Clegg et al. 1992).

109   **THE GORGON SLIDE**

110   *General Characteristics*

111   The Gorgon Slide was evacuated from a failed slope that defines part of the present-day shelf-edge of

112   NW Australia (Fig. 1). It was deposited in the adjacent Kangaroo Syncline, forming a lenticular, NW-SE

113   trending feature that wedges-out to the SE (against the continental slope) and to the NW (against the

114   eastern margin of the Exmouth Plateau Arch) (see Figs. 1B-C and 2). The slide has a maximum runout

115   distance of *c.* 70 km. It is up to 500 m-thick and has a total volume of *c.* 500 km^3 (Fig. 3A) (Nugraha et

116   al. 2019a). The slide terminates against two lateral margins (to the NE and SW), it is *c.* 30 km-wide in

117   the central part and abruptly narrows to *c.* 18 km at its frontal end (Fig. 3A). These width changes form

118   two frontal margins (eastern and western), that are separated by a NW-SE trending, *c.* 10 km-long

119   lateral margin (Fig. 3A). The central and frontal parts of the slide display a notable along-strike change

120   in seabed rugosity, which defines two distinctive regions: Areas A and B (Fig 3B). Area A comprises a

121   highly rugose seabed, indicated by frequent changes of dip, and is bound by the NE lateral and eastern

122   frontal margins (Fig. 3B). Area B comprises a relatively less rugose seabed and is bound by the SW

123 lateral and western frontal margins (Fig. 3B). Areas A and B are separated by a linear, NW-SE trending

124 feature (see zoomed-in image in Fig. 3B), which is subparallel to both lateral margins of the slide. This

125 linear feature is narrow (*c.* 170-300 m-wide) and extends for *c.* 26 km, from its updip limit to the point

126 where it merges with Area B lateral margin (see Figs. 3B-C). This feature marks the change of seabed

127 relief between Areas A and B, where the vertical difference of relief between the two areas are

128 variable downdip, ranging from *c.* 10 m to *c.* 20 m (Fig. 3C).

129 The Gorgon Slide originated from a steeply-dipping (*c.* 30°), *c.* 350 m-high headwall scarp, which forms

130 a *c.* 18 km-long evacuation zone (Fig. 4A). The frontal margin of Area A is clearly marked by positive

131 seabed relief (*c.* 30 m) relative to the smooth seabed bounding pre-existing strata immediately

132 downdip. The Gorgon Slide and the pre-existing strata share similar chaotic and transparent seismic

133 facies. Thus, the pre-existing strata are interpreted as an older MTC (Fig. 4A). A strike seismic section

134 of the Gorgon Slide exhibits the following along-strike lateral boundaries (Fig. 4B): (i) the SW lateral

135 margin defines the pinch-out of the slide onto substrate, and (ii) the NE lateral margin that marks the

136 boundary with the older MTC. Sub-parallel, continuous reflections on top of the older MTC are cross-

137 cut and overlain by overspill of the slide. Thus, these reflections are interpreted as 'paleo-seabed' (Fig.

138 4B). The morphology of the basal-shear surface appears to mimic that of the underlying substrate in

139 most of Area B in the SW (Fig. 4B). In Area A, the basal-shear surface truncates underlying seismic

140 reflections and its gradient becomes flatter adjacent to the NE lateral margin.

141 The linear zone on the seabed (see Figs. 3B-C) is interpreted as a longitudinal shear zone (*sensu* Bull

142 et al. 2009), which records internal variations of transport velocity within an MTC. Occasionally, the

143 longitudinal shear zone not only defines the change of seabed relief between Areas A and B, it could

144 also coincide with positive seabed relief (see Fig. 4B).

145 The internal character of the Gorgon Slide is variable, and a seismic facies classification is used to

146 capture this internal heterogeneity (Fig. 5). This classification captures variations in both strain and

147   degree of internal disaggregation (i.e. flow rheology) within the MTCs (e.g. Alves et al. 2014). It builds

148   on previous studies that have calibrated seismic reflection data with lithology from well data (e.g.

149   Sawyer et al. 2009), as well as seismic reflections forward modelling using outcrops (Dykstra et al.

150   2011). Five seismic facies (SF) are defined in this study (Fig. 5A) based on variability in internal

151   reflection configurations, both in cross-section and plan-view (see Figs. 5B-G): (i) SF-1 - mostly

152   transparent with low-to-variable amplitude reflections, which are interpreted as debrites (cf.

153   Posamentier and Kolla 2003; Posamentier and Martinsen 2011; Ortiz-Karpf et al. 2017); (ii) SF-2 -

154   contains low-to-medium amplitude, discontinuous folded reflections in cross-section that occasionally

155   forms sinuous lineations in plan-view, and also interpreted as debrites with partially disaggregated

156   material; (iii) SF-3 - contains high-amplitude folded reflections that are offset by thrusts, interpreted

157   as fold and thrust systems; (iv) SF-4 is characterised by isolated packages of coherent, sub-parallel

158   reflections within a matrix composed of SF-1 and 2, interpreted as megaclasts transported within

159   debritic matrix (cf. McGilvery 2004; Bull et al. 2009; Jackson 2011; Ortiz-Karpf et al. 2017; Hodgson et

160   al. 2018); and (v) SF-5 is composed of sub-parallel and continuous reflections that characterise non-

161   MTC seismic facies, i.e. progradation beneath the shelf and layered slope strata within the evacuation

162   zone (see Fig. 4A) (e.g. Prélat et al. 2015). Internal seismic facies of the longitudinal shear zone is

163   generally characterised by SF-1 (Fig. 3C), indicating highly disaggregated materials within the zone due

164   to intense shearing (cf. Ogata et al. 2014; Bull and Cartwright 2019; Omeru and Cartwright 2019).

165   However, its relatively subtle width means that the internal seismic facies are often undifferentiated

166   from adjacent MTC bodies (Figs. 4B, and 5B-E).

167   To reconstruct emplacement processes, the Gorgon Slide is synthesized in terms of its kinematic

168   indicators and internal seismic facies from four domains: (i) headwall; (ii) upper translation (UTD); (iii)

169   lower translation (LTD); and (iv) toe (see Fig. 3B).

171   Besides the main headwall scarp, features observed in the headwall domain (see Fig. 6) include a small

172   scarp, circular depressions, and linear depressions updip from the main headwall scarp (see zoomed-

173   in image in Fig. 6A). The small scarp (*c.* 10 m-high) is likely to be older than the main headwall scarp

174   due to their cross-cutting relationship (Fig. 6B). The circular depressions have a diameter of *c.* 100 to

175   300 m, which are mainly distributed within the small scarp area. They are interpreted as pockmarks

176   (e.g. Hengesh et al. 2013; Scarselli et al. 2013), which would indicate active fluid venting. The linear

177   depressions are *c.* 3 to 5 km-long and *c.* 15 m-deep, which are interpreted as crown cracks possibly

178   marking the location of future slope failure (Varnes 1978; Frey-Martinez et al. 2005).

179   In between the main headwall scarp and the evacuation-deposition zone boundary, within the

180   evacuation zone, there are *c.* 5-16 km-long elongate features (Figs. 6A-B) with v-shaped geometries

181   (*c.* 150-300 m-wide and *c.* 10-25 m-deep, see zoomed-in image in Fig. 6B). We interpret them as

182   grooves (*sensu* Bull et al. 2009) that were formed due to tooling of failed materials (e.g. megaclasts)

183   into the substrate during transport (Posamentier and Martinsen 2011; Ortiz-Karpf et al. 2017;

184   Hodgson et al. 2018; Sobiesiak et al. 2018). Based on their orthogonal relationship with the headwall

185   scarp, these grooves are a reliable indicator of the translation pathway of the slide through the

186   evacuation zone.

187   The initial failed volume of the Gorgon Slide that was removed from the headwall domain ranges from

188   31 to 43 km^3, which is 12-16 times smaller than the deposited volume (*c.* 500 km^3) (Nugraha et al.

189   2019a). This volume discrepancy is interpreted as a result of significant erosion and substrate

190   entrainment of the carbonate ooze substrate during transport (see Nugraha et al. 2019a).

192   **Basal-shear surface.–** Grooves observed in the updip part of the upper translation domain (Fig. 7A),

193   are a continuation of those within the evacuation zone (see Fig. 6), displaying similar dimensions and

194   geometries (see Headwall domain section). However, the grooves in this domain converge downslope

195   towards the NE lateral margin (Fig. 7A), which contrasts to the more commonly described downslope-

196   diverging grooves (e.g. Posamentier and Kolla 2003; McGilvery 2004; Ortiz-Karpf et al. 2017). This

197   geometry implies that the pathway of the slide was focused towards the steep, NE lateral margin. As

198   a result, the slide is thickest adjacent to this lateral margin (see Fig. 3A). The pathway was likely

199   controlled by the morphology of the basal-shear surface that broadly follows the morphology of the

200   underlying substrate (see Fig. 4B). This supports the observations of Ortiz-Karpf et al. (2017), who

201   stress the impact of precursor morphology on the emplacement of MTCs.

202   In the central part of the basal-shear surface, there is a pair of NW-SE trending, curved lineations

203   across the upper translation domain (Fig. 7A). They bound an area that is shallower than its

204   surrounding area (shaded grey in Fig. 7A). These lineations appear to mark subtle changes (*c.* 10 m) in

205   the depth of the basal-shear surface. We interpret these lineations as 'ramps' bounding an area called

206   a 'flat' (Trincardi and Argnani 1990; Lucente and Pini 2003; Frey-Martinez et al. 2005; Bull et al. 2009).

207   The ramps record basal erosion by the overlying slide that are commonly expressed by truncated

208   reflections of underlying substrate by a basal-shear surface (e.g. Bull et al. 2009). However, as the

209   ramps in this domain represent relatively small steps (i.e. 10 m), the basal-shear surface does not

210   truncate more than one reflector.

211   Adjacent to the NE lateral margin, there is an area comprising highly discontinuous reflections on the

212   variance map (Fig. 7A). Some of these discontinuous reflections form lineations oriented oblique to

213   the NE lateral margin. This area is characterised by low-to-medium amplitude, discontinuous

214   reflections at, and immediately beneath, the basal-shear surface (Fig. 7D). We interpret the substrate

215   in this area to have been compressionally deformed due to stress exerted by the slide, forming a

216   'basal-shear zone' (Butler and McCaffrey 2010; Hodgson et al. 2018; Cardona et al. 2020).

217   On top of the older MTC, there is a series of lineations (0.5 to 1.5 km-long) that originate from the NE

218   lateral margin (Figs. 7A and D). These lineations are oriented at *c.* 45° relative to the NE lateral margin.

219   We interpret these lineations as shear fractures (i.e. Riedel shears) that developed due to strike-slip

220   movement along the NE lateral margin. This implies that the Gorgon Slide exerted stress onto the

221   older MTC during transport (e.g. Fleming and Johnson 1989; Martinsen 1994; Fossen 2016).

222   Northwestwards transport of the Gorgon Slide implies that the NE lateral margin represents a dextral

223   strike-slip fault of the Gorgon Slide relative to the older MTC (Fig. 7A). Fleming and Johnson (1989)

224   suggest that this type of fractures is developed during an early stage of strike-slip faulting along lateral

225   margin of the MTCs, prior to the formation of through-going lateral margins. They recorded fractures

226   oriented at 45° clockwise from the trend of a dextral lateral margin, similar to the shear fractures

227   found in our study.

228   **Internal body.–** The proximal part of the upper translation domain is dominated by SF-1 that

229   surrounds scattered megaclasts (SF-4) (Fig. 7B). These megaclasts have elliptical to rectangular

230   geometry in map-view, with long-axis lengths ranging from *c.* 0.18 to 1 km and thickness of *c.* 70 to

231   140 m (Fig. 7B). Seismic sections show that these megaclasts are sometimes internally folded and

232   faulted (Fig. 7D). In the central part of this domain, the megaclasts are concentrated, forming a *c.* 15

233   km-long and 3 km-wide, convex-upslope cluster of megaclasts. This cluster is bound by a gradational

234   boundary with SF-1 in the E, and an abrupt boundary in the W, which is defined by the longitudinal

235   shear zone (Fig. 7B). Most of this cluster occurs within Area A, with a subsidiary megaclasts cluster

236   observed within Area B, *c.* 5 km downdip (Fig. 7B). These clusters share similar frequency expressions

237   on spectral decomposition map (Fig. 8A), and internal reflections and thicknesses (Figs. 8B-C), and are

238   separated by the longitudinal shear zone.

239 Immediately downdip from the central part of the Area A megaclast cluster, partially-disaggregated

240 materials contained within SF-2 are aligned to form a series convex-upslope bands (Fig. 7B). These

241 bands are sub-parallel to the geometry of the cluster (Figs. 7B and 8A). In contrast, downdip from the

242 eastern margin of the cluster, the bands show a convex-downslope geometry terminating at the NE

243 lateral margin (Figs. 7B and 8A). A NW-SE trending, narrow area (*c.* 500 m-wide and *c.* 10 km-long) of

244 SF-1 defines the boundary between these two sets of bands (Fig. 7B). There is a similar occurrence of

245 convex-downslope bands downdip from the cluster in Area B (Fig. 7B). In seismic section, these bands

246 are expressed as low-frequency, medium-amplitude folded reflections (Fig. 7D).

247 The scattered megaclasts in the proximal part of this domain are clustered, possibly due to downslope-

248 convergence of the pathway of the Gorgon Slide based on the orientation of the grooves on the basal-

249 shear surface (see Fig. 7A). The clusters of megaclasts in Areas A and B are interpreted to have been

250 initially emplaced as a single cluster. Subsequently, they were cross-cut by the longitudinal shear zone,

251 which was also initiated at this area (Fig. 7B).

252 The clusters of megaclasts were likely induced internal velocity perturbations within the slide during

253 transport. This internal velocity variation is evidenced by the convex-downslope shear bands, in both

254 Areas A and B, which are located downflow from the convex-upslope shear bands adjacent to the

255 cluster of megaclasts in Area A (Fig. 7B). Another indicator of internal velocity variations is the narrow

256 area within Area A that separates the convex-downslope and -upslope shear bands (Fig. 7B). This area

257 is interpreted as an 'internal shear zone' (cf. Ogata et al. 2014; Bull and Cartwright 2019; Omeru and

258 Cartwright 2019), containing disaggregated material due to intense shearing. Other studies have also

259 discussed how the entrainment and abrasion of megaclasts during transport of MTCs could affect flow

260 rheology (e.g. Joanne et al. 2013; Ortiz-Karpf et al. 2017; Hodgson et al. 2018; Sobiesiak et al. 2019),

261 and therefore variations in intra-MTC flow velocity.

262   **Top surface.–** The top surface of the Gorgon Slide sometimes enhances the appearance of some

263   features recorded within the internal body (Fig. 7C). For example, the internal shear bands are

264   expressed as ridges with positive seabed relief. These ridges are terminated at the longitudinal shear

265   zone between Areas A and B, and change their orientations (from convex-upslope to -downslope) at

266   the internal shear zone (see Figs. 7C and 8). These ridges are interpreted as a secondary flow fabric

267   (*sensu* Bull et al. 2009), suggesting flow velocity variation within the slide.

268   *Lower translation domain*

269   **Basal-shear surface.–** The majority of kinematic indicators observed in the upper translation domain

270   extend to this lower translation domain (i.e. ramp, deformed substrate and shear fractures; Fig. 9A),

271   apart from the absence of grooves. Here, the ramps are deeper (*c.* 20 m-deep, Fig. 9D), and lineations

272   within the deformed substrate area are more apparent on the variance map (Fig. 9A). Downflow from

273   the deformed substrate, there are SE-facing ramps (i.e. perpendicular to transport direction) that

274   merge with the ramp that extends from the upper translation domain (Fig. 9A). Adjacent to the

275   deformed substrate, there is a concentration of shear fractures that diminish downdip.

276   The ramps, deformed substrate, and shear fractures indicate that erosion and deformation also

277   occurred in this lower translation domain (Fig. 9A). There is a close spatial relationship between the

278   deformed substrate and the concentration of shear fractures (Fig. 9A), which also coincides with the

279   thickest slide occurrence in Area A (Fig. 3A). This could imply that the basal and lateral substrate

280   deformation was more severe due to increased stress exerted by the thickest part of the Gorgon Slide.

281   However, Cardona et al. (2020), concluded from an outcrop study that there is no statistical

282   correlation between the intensity of deformation of the basal-shear zone and the thickness of the

283   overlying MTC.

284   **Internal body.–** The convex-upslope shear bands, between the longitudinal and internal shear zones

285   within Area A, diminish downflow (Fig. 9B). In contrast, the convex-downslope shear bands within

286   Area B continue and are more prominent in this lower translation domain (Fig. 9B).

287   Adjacent to the NE lateral margin, there is another cluster of megaclasts (Fig. 9B). In seismic section

288   (Fig. 9D), this cluster contains megaclasts that have similar facies to those in the upper translation

289   domain (Figs. 7D and 8B-C). However, these megaclasts have shorter long-axis (*c.* 0.05 to 0.54 km) and

290   are thicker (*c.* 73 to 220 m) than those in the upper translation domain, i.e. *c.* 0.17 to 0.98 km-long

291   and *c.* 70 to 137 m-thick (see Fig. 10A). Also, the megaclasts in the upper and lower translation

292   domains show different trends of their long-axis (Fig. 10B). The megaclasts in the upper translation

293   domain are generally trending NE-SW, and the ones in the lower translation domain are trending

294   NNW-SSE. We also found megaclasts that are concentrated in the basal part of the slide, which are

295   (see Fig. 9D): (i) containing chaotic and transparent internal reflections, (ii) bound by folded top, and

296   (iii) underlain by a ramp. We name them as 'basal megaclasts'.

297   The presence of longitudinal and internal shear zones suggest that internal variation of flow velocity

298   continued to occur in this domain (Fig. 9B). Between these shear zones, the gradual downflow

299   disappearance of the convex-upslope shear bands suggests a decrease in internal velocity

300   perturbations induced by the cluster of megaclasts in upper translation domain (see Fig. 7B).

301   The cluster of megaclasts adjacent to the NE lateral margin (Figs. 9B and D) are located immediately

302   downflow from, and have similar width (2.5 km) to, the deformed substrate area (Fig. 9A). Thus, the

303   basal and lateral substrate deformations documented on the basal-shear surface (Fig. 9A) could be

304   related to this cluster of megaclasts, instead of reflecting the maximum thickness of the Gorgon Slide

305   (Fig. 3A). This interpretation is supported by the same observation from the Rapanui MTD (Cardona

306   et al. 2020), where the thickness of the deformed substrate is correlated to higher concentrations of

307   rafted blocks (i.e. megaclasts), and not the thickness of overlying MTC. The higher concentration of

308   megaclasts indicates an increase in flow competence overriding the area of the deformed substrate.

309   In addition, the long-axis orientations of the megaclasts in the lower translation domain are generally

310   oblique to sub-parallel, in contrast to the ones in the upper translation domain that are generally

311   perpendicular, to the transport direction (Fig. 10B). Their long-axis orientations are likely to be

312   controlled by velocity gradients (Mazzanti and De Blasio 2010), where the megaclasts in the lower

313   translation domain are adjacent to the NE lateral margin, and experienced abrupt change of velocity

314   gradient as they moved against the stationary older MTC (Fig. 9B). In contrast, the cluster of

315   megaclasts in the upper translation domain experienced a lower velocity gradient, which then formed

316   the convex-upslope geometry (Fig. 7B).

317   The basal megaclasts have transparent internal facies and display folded tops (Fig. 9D). We suggest

318   they are more deformed compared to the adjacent megaclasts (Fig. 9D). Their transparent internal

319   facies could be related to intense shearing during transport (Alves 2015; Gamboa and Alves 2015), and

320   the folded top may be formed due to impingement of the megaclasts by the slide against the

321   underlying ramp (see Fig. 9D) (Jackson 2011). This impingement is expressed as a positive relief of the

322   seabed (Fig. 9D).

323   **Top surface.–** The top surface shows that the internal shear zone merges with the longitudinal shear

324   zone in the distal part of the lower translation domain (Fig. 9C). These shear zones outline an area

325   covering convex-upslope ridges that narrows and diminishes downflow. Consequently, Area A

326   becomes dominated by the convex-downslope ridges (Fig. 9C). However, we can see that immediately

327   downflow from the merging point of the shear zones, the ridges in Area A have convex-upslope

328   geometries, most notably adjacent to the longitudinal shear zone (Fig. 9C).

329   The top surface supports the interpretation of kinematic indicators within the internal body of the

330   slide (Figs. 9B-C). Here, it is also evident that velocity perturbation induced by the cluster of megaclasts

331   in upper translation domain (Figs. 7B and 8A) had decreased, and diminished downflow, as clearly

332   marked by the merging of the two shear zones (Fig. 9C). However, downflow from the merging point,

333   the presence of convex-upslope ridges within Area A (terminating at the longitudinal shear zone)

334   suggest that internal velocity perturbations continued to occur (Fig. 9C).

335   *Toe domain*

336   **Basal-shear surface.–** The basal-shear surface in this domain serves as the frontal margin of Area A,

337   and swings through 90° to join the lateral margin of Area B that continues downdip, beyond the 3D

338   seismic reflection data area (Fig. 11A). The deformation style of the substrate (Fig. 11A) resembles

339   that of the upper and lower translation domains (see Figs. 7A and 9A). In the SW part of this domain,

340   there is a *c.* 30 m-high ramp (Figs. 10A and D), which is more profound than that in the lower

341   translation domain (*c.* 20 m).

342   The geometry of the basal-shear surface indicates that Area B extends further downdip than Area A

343   (Fig. 11A). The deformed substrate and the ramp indicate that substrate deformation and erosion

344   continued to occur beneath the main body of the slide, despite being located the furthest from the

345   headwall.

346   **Internal body.–** SF-1 and SF-3 (i.e. folds and thrusts system) dominate the distal part of Area A and B,

347   respectively (Fig. 11B). The thrusts within Area B dip to the SE, sub-parallel to the transport direction

348   of the slide (see Figs. 5G and 11B and D).

349   Within the older MTC (see Fig. 11B), there is a cluster of megaclasts (*c.* 2.5 km-wide and *c.* 5 km-long).

350   The SE and SW margins of this cluster of megaclasts are defined by Area A frontal margin and Area B

351   lateral margin, respectively (Fig. 11B). Within the cluster of megaclasts, there are lineations (NNW-SSE

352   trending) that are broadly perpendicular to the orientation of the Area A frontal margin and the

353   thrusts within Area B (i.e. NE-SW trending). In seismic section, these megaclasts are characterised by

354   medium-amplitude sub-parallel reflections at the base, which become folded towards the top (Fig.

355   11D). The internal reflections are separated by NE-dipping thrusts. The lineations on the time-slice

356   (Fig. 11B) correspond to these thrusts. Thus, we name this cluster of megaclasts as 'thrusted

357   megaclasts'.

358   Abrupt truncation of the thrusted megaclasts by the frontal margin of Area A, and the thrusts within

359   Area B, suggests a cross-cutting relationship (Fig. 11B). Thus, we interpret that the thrusted megaclasts

360   had been emplaced at their present location prior to the emplacement of the Gorgon Slide. Some

361   thrusted megaclasts (i.e. indicated by high RMS amplitude) are observed within the frontal part of

362   Area A (Fig. 11B). However, these thrusted megaclasts are distinctly different from those of the thrust

363   system within Area B (Fig. 11D). This suggests that the thrusted megaclasts were only entrained by

364   the Gorgon Slide in the frontal part of the Area A (Fig. 11B). In contrast, the Area B lateral margin

365   developed along the SW margin of the thrusted megaclasts, without any evidence of entrainment of

366   the thrusted megaclasts by the slide within Area B.

367   The longitudinal shear zone that extends from the upper translation domain (see Figs. 7A and 8A) joins

368   Area B lateral margin in the toe domain (Fig. 11B). This may indicate a relationship between the

369   thrusted megaclasts and inferred intra-MTC velocity perturbation. Specifically, the velocity

370   perturbation could have originated from the SW margin of the thrusted megaclasts (i.e. Area B lateral

371   margin) and propagated upflow (Fig. 11B). Therefore, this velocity perturbation caused by the

372   thrusted megaclasts connected with the downflow-propagating velocity perturbation induced by the

373   cluster of megaclasts in the upper translation domain (Figs. 7B and 8A). Frey-Martínez et al. (2006)

374   also observed similar role of pre-existing blocks (megaclasts), where a single MTC flow bifurcates to

375   form two flows with different transport directions.

376   **Top surface.–** The rugose seabed with *c.* 30 m-high ridges relative to the flat seabed above the older

377   MTC defines the frontal margin of Area A (see Fig. 11C). The vertical relief of the ridges of Area A is

378   higher than in both Area B (*c.* 10 m, Fig. 11C) and the lower translation domain (*c.* 10 m, Fig. 9).

379   The ridges at the Area A frontal margin could indicate a buttressing effect of the slide against the

380   thrusted megaclasts (Fig. 11C), which then formed ridges that decrease in height upflow. In contrast,

381   the ridges in Area B are not as high as those in Area A. Thus, the slide was not buttressed against the

382   thrusted megaclasts and it translated further downdip (Fig. 11C). These differential processes in the

383   toe domain of Areas A and B reflect the merging between Area B lateral margin and the longitudinal

384   shear zone (Fig. 11C).

385   **DISCUSSION**

386   *Emplacement processes of the Gorgon Slide: a multi-cell flow emplacement mechanism*

387   A multiple flow cell model based on field studies has been proposed by Alsop and Marco (2014), who

388   advance the notions of Farrell (1984) of a large single-cell flow model that controls deformation

389   patterns within an MTC. They suggest that a large (first-order) MTC consists of a number of smaller

390   (second-order) flow cells formed during emplacement of the MTC. These smaller flow cells may

391   interact with each other and cause overprinting on initially formed structures. Interaction between

392   flow cells has also been documented from sonar (e.g. Prior et al. 1984; Masson et al. 1993; Gee et al.

393   2001) and 3D seismic reflection data (e.g. Bull et al. 2009; Steventon et al. 2019), and captured in the

394   form of primary (longitudinal shear zone) and secondary (sinuous shear bands) flow fabrics (*sensu* Bull

395   et al. 2009). These kinematic indicators indicate differential speeds and/or timing of downslope

396   translating material (Masson et al. 1993; Gee et al. 2005).

397   In this study, the Gorgon Slide appears to comprise two intra-MTC (second-order) flow cells. These are

398   represented physically by Areas A and B, and for the purpose of this process-based interpretation are

399   re-named as Cells A and B, respectively. The emplacement processes of the Gorgon Slide are captured

400   in a schematic model that recognises three stages of development (Fig. 12).

401   **Stage 1.–** Prior to slope degradation, a surface rupture might have been triggered by two main factors

402   (Fig. 12A). First, the normal faults bounding the horst could have been inverted due to compression

403 to destabilise the slope (Keep et al. 1998; Nugraha et al. 2019b). Second, the existence of pockmarks

404 observed on the seabed (see Fig. 6) implies that there has been active fluid venting in the headwall

405 area (Hengesh et al. 2013), most likely originating from the deeper gas-bearing horst block of the

406 Gorgon Field (Fig. 2). Gas leakage into shallower sediments could have lowered the shear strength of

407 these sediments, and primed the slope for subsequent failure (Scarselli et al. 2013). However, the

408 Gorgon Slide was not an isolated occurrence, but rather the most recent. Previous collapse of the

409 continental margin is reflected in the older (pre-Gorgon) MTC, which would have left a remnant

410 topography both on the slope but especially in the area of subsequent Gorgon Slide deposition. Most

411 notably, thrusted megaclasts had already been emplaced in the vicinity of the future toe domain of

412 the Gorgon Slide (Fig. 12A).

413 **Stage 2.–** The arcuate geometry of the main headwall scarp indicates that the failed sediments were

414 evacuated during a single mass-transport event (see Fig. 6). The evacuated sediments might include

415 megaclasts derived from either the headwall and/or entrained from the layered slope substrate (Figs.

416 11B and 4A). During translation, the megaclasts could be deformed and fragmented (e.g. Gee et al.

417 2005; Alves 2015).

418 The downslope-converging grooves within the headwall and upper translation domains suggest a

419 convergent pathway of the slide, resulting in the clustering of the megaclasts (Fig. 12B). In the lee-side

420 of the cluster of megaclasts, the following features were formed: (1) convex-upslope shear bands

421 within the slide, and (2) convex-upslope ridges on top of the slide. These features indicate slower

422 transport velocity in and around the area of concentrated megaclasts (Fig. 12B). Higher transport

423 velocities of flows moving around the megaclast-rich area led to the formation of the longitudinal

424 shear zone, and the initiation of Cells A and B. The cluster of megaclasts effectively acted as an obstacle

425 to the initial, single-cell flow. Other studies have also documented such mechanism, where the

426 geometry of shear bands and ridges of MTCs downslope from translating megaclasts suggest slower-

427   moving flows than surrounding materials (e.g. Masson et al. 1993; Lastras et al. 2005; Gee et al. 2006;

428   Bull et al. 2009).

429   **Stage 3.–** The downslope propagation of the basal-shear surface was coupled with the evolution of

430   the internal body and top surface of the slide. The area covering the convex-upslope shear bands and

431   ridges narrowed downslope (Fig. 12C), which suggests a reduction in the influence of the cluster of

432   megaclasts on slowing down the flow of material in its lee-side. Thus, we interpret this area as a

433   'shadow zone'. The shadow zone is bound by the longitudinal shear zone separating the two cells, and

434   the internal shear zone within Cell A (Fig. 12C). The shadow zone is an example of how megaclasts

435   influence flow processes of an MTC (e.g. Masson et al. 1993; Lucente and Pini 2003; Jackson 2011;

436   Hodgson et al. 2018).

437   Downflow from the shadow zone, ridges of Cell A show convex-upslope geometries adjacent to the

438   longitudinal shear zone. In contrast, ridges of Cell B consistently exhibit convex-downslope geometries

439   (Fig. 12C). These geometries indicate that Cell A resisted the downslope translation of Cell B. As a

440   result, the ridges of Cell A were dragged downslope, and the ridges of Cell B were dragged upslope

441   (Fig. 12C). Therefore, we suggest that Cell A was travelling more slowly than Cell B. Furthermore, the

442   high seabed relief of Cell A at the frontal margin suggest that it was forced to stop its translation by

443   the pre-existing thrusted megaclasts (Fig. 12C), and, thus, can be considered as "stopping structures"

444   that were formed during cessation (Masson et al. 1993; Gee et al. 2006). In contrast, the position of

445   the thrusted megaclasts allowed Cell B to translate further downdip than Cell A. Thus, Cell B was not

446   only travelled faster, but also further, than Cell A.

447   *Impact of flow cells formation on MTCs flow behaviour*

448   Submarine debris flow can travel for tens to hundreds of km across low gradient (*c.* <1°) continental

449   slope, despite its cohesive nature (Gee et al. 1999; Lastras et al. 2005). This mobility can be explained

450   by, for instance, sustained pore-fluid pressure within the flow during transport (Major and Iverson

451   1999; McArdell et al. 2007), and also the presence of a thin lubricating layer of fluid at the base of the

452   frontal part of the flow (i.e. hydroplaning, Mohrig et al. 1998). Ultimately, a debrite is formed by *en*

453   *masse* freezing of the debris flow (e.g. Talling et al. 2012), where materials at flow margins (i.e. frontal

454   and lateral) cease moving first, followed by materials in the main body of the flow (Iverson 1997).

455   The Gorgon Slide provides evidence of how a mass flow split into two smaller flow cells (Cell A and B,

456   Fig. 12). The relationship between the two cells suggests that Cell A ceased movement, while Cell B

457   was still in motion. This suggests that *en masse* freezing did not occur across the entire body of the

458   flow synchronously. Instead, individual flow cells underwent differential timing of freezing, resulting

459   in different runout distance of the cells. We propose that lateral friction and related pore-fluid

460   pressure played an important role in controlling the runout distance of the two cells, in addition to

461   the presence of pre-existing thrusted megaclasts. The longitudinal shear zone may have sustained

462   excess pore-fluid pressure between the two cells, such that low friction between the two cells could

463   be maintained, allowing Cell B to keep in translation despite the impediment by Cell A. In contrast,

464   pore-fluid pressure was likely to dissipate at the lateral margins during translation (e.g. NE lateral

465   margin, Fig. 3). The lack of excess pore-fluid pressure would have resulted in high friction between the

466   moving slide (e.g. Cell A) and stationary lateral substrate (i.e. the older MTC). This high friction at the

467   lateral margin was likely to reduce runout distance more significantly than the friction at the

468   longitudinal shear zone. Such mechanisms are also observed from experimental studies (Major and

469   Iverson 1999; De Haas et al. 2015).

470   Our results suggest that a debris flow comprising smaller flow cells could experience a 'punctuated'

471   freezing, where a flow cell can have shorter runout distance than the others, resulting from differential

472   friction and pore-pressure dissipation at flow cells margins. The flow behaviour documented in our

473   study may be considered for modelling the potential impact of MTCs on subsea infrastructures.

Controls on flow cell formation

475   Flow cell formation within an MTC depends on internal velocity perturbations, which are controlled

476   by variations in at least three local factors (Farrell 1984; Alsop and Marco 2011; Alsop and Marco

477   2014): (i) lithology and/or geometry of stratigraphic element (e.g. MTCs, channels and lobes); (ii) fluid

478   pressures within the MTC and/or substrate; and (iii) slope and/or geometry of basal-shear surface

479   underlying the MTC.

480   In the Gorgon Slide, a cluster of megaclasts within a debritic matrix initiated flow cell formation. This

481   implies that lithology, in particular variations of the degree of disaggregation within the slide, play a

482   key role in forming the two seismic-scale flow cells. In addition, the geometry of the basal-shear

483   surface was also important in converging the flow, clustering the megaclasts, initiating velocity

484   perturbation, and terminating the flow cells. Those three local variations (i.e. lithology, fluid pressures,

485   and basal-shear surface geometry) may have been influential prior to emplacement, but their

486   properties could also evolve during translation and cessation of the parent flow (Iverson 1997; Dykstra

487   et al. 2011; Joanne et al. 2013; Alsop and Marco 2014; Ortiz-Karpf et al. 2017; Hodgson et al. 2018).

488   *Origin of the pre-existing thrusted megaclasts*

489   We have established that the thrusted megaclasts are encased by the older MTC, and, thus, had

490   existed in their present position prior to the Gorgon Slide emplacement. Here, we discuss possible

491   origins of the thrusted megaclasts. Deformations within, and the present location of, the thrusted

492   megaclasts might indicate that they are either *in-situ* (remnant) or translated megaclasts.

493   Relatively continuous, sub-parallel reflections at the base of the thrusted megaclasts could indicate

494   that they had not been translated (Fig. 11D). This might support the interpretation that they are *in-*

495   *situ* megaclasts. However, the NE-dipping thrusts originating from the base, and folded reflections

496   toward the top of the megaclasts, record contractional strain as a result of broadly NE-SW trending σ_1

497   stress (Fig. 11D). This stress was unlikely exerted by the Gorgon Slide onto the *in-situ* megaclasts, as

498   the Gorgon Slide was transported towards the NW. Likewise, it is unlikely that the NE-dipping thrusts

499   were formed by an older MTC that translated to the SW. This is because there is no possible source of

500   MTCs towards the NE (see location of the NW Australian shelf, Fig. 1A).

501   If the thrusted megaclasts were to be deformed or translated by an MTC, the MTC should be sourced

502   either from the Exmouth Plateau Arch (i.e. to the SW from the megaclasts) or from the NW Shelf of

503   Australia (see Fig. 1A). As the thrusts of the megaclasts are NE-dipping (Fig. 11D), the thrusted

504   megaclasts are unlikely to be deformed or translated by a NE-flowing MTC originated from the arch.

505   This MTC should produce SW-dipping thrusts. Thus, the MTC forming the thrusted megaclasts was

506   more likely sourced from the NW Shelf, similar to the source of the Gorgon Slide. However, a NW-

507   flowing MTC should generate SE-dipping thrusts, instead of NE-dipping thrusts. This fact suggests that

508   the thrusted megaclasts are unlikely to be deformed *in-situ*. Thus, thrusted megaclasts might be

509   deformed during translation within the NW-flowing MTC, rotated counter-clockwise (*c.* 70-80°) and

510   then rested at their present location.

511   The thrusted megaclasts have similar dimensions (Figs. 13A-B) and seismic facies (Figs. 13C-D), to the

512   basal megaclasts (see Lower translation domain section, Fig. 9D). Thus, it is possible that the thrusted

513   megaclasts were deformed and translated by the NW-flowing MTC. Deformation and rotation of

514   megaclasts during MTC translation have been documented in other studies, such as in Storegga Slide

515   (Bull et al. 2009). Here, the megaclasts were re-oriented from perpendicular to become sub-parallel

516   to transport direction with increasing distance from headwall scarp.

517   **CONCLUSIONS**

518   We use 3D seismic reflection data covering a recent mass-transport complex (MTC), the Gorgon Slide,

519   from the Exmouth Plateau, offshore NW Australia, to investigate how flow cells within an MTC was

520   formed, translated, and finally ceased. This study concludes that:

521   1. The Gorgon Slide was evacuated from a steep, NE-SW trending, *c.* 350 m-high headwall scarp

522   and transported towards the NW. Layered slope strata in this headwall domain are the likely

523   source of megaclasts that are subsequently transported downslope.

524   2. In the proximal part of the translation domain, downslope-converging grooves on the basal-

525   shear surface indicate that the pathway of the slide was focused towards its lateral margin in

526   the NE. The convergent pathway of the flow results to the clustering of the megaclasts, whose

527   long-axes are generally trending NE-SW, perpendicular to the transport direction. This cluster

528   of megaclasts became an obstacle to flow, causing velocity perturbation within the slide. The

529   velocity perturbation is recoded within the internal body by convex-upslope shear bands, and

530   on the seabed by convex-upslope ridges. These features indicate slower transport velocity of

531   the cluster of megaclasts and materials in its lee-side. The area of the slower-moving materials

532   narrows downslope, indicating that velocity perturbation caused by the cluster of megaclasts

533   gradually diminished downflow, forming a 'shadow zone'. Transport velocities of flows were

534   higher around the megaclasts, resulting in the formation of longitudinal shear zone and the

535   initiation of two flow cells, namely Cells A and B.

536   3. In the distal part of the translation domain, kinematic indicators recorded on the basal-shear

537   surface indicate that erosional and deformational processes occurred. Erosional processes are

538   evidenced by ramp, and deformational processes are evidenced by deformed substrate or

539   basal-shear zone and shear fractures adjacent to the NE lateral margin. The deformed

540   substrate and shear fractures are closely related to the thickest part of the slide, comprising a

541   cluster of megaclasts, with individual megaclasts generally trending NNW-SSE, oblique to sub-

542   parallel to the transport direction. Shear bands within the slide and ridges on the seabed of

543   Cell A were dragged downslope, while those of Cell B were dragged upslope. This points to

544   Cell A acting as an impediment to the movement of faster-moving Cell B.

545   4. In the toe domain, the frontal margin of Cell A is marked by positive seabed relief (*c.* 30 m-

546   high) that gradually decreases upflow, which is significantly higher than the relief of Cell B (*c.*

547   10 m-high). This suggests that Cell A was buttressed against a pre-existing cluster of

548   megaclasts (i.e. encased by older MTC), while Cell B was not. Therefore, as there were no flow

549   obstacles, Cell B was able to travel further than Cell A.

550   5. The morphology of the basal-shear surface and the degree of disaggregation within the slide,

551   especially the megaclasts, played important roles in flow cell evolution. The basal-shear

552   surface controlled the pathway of the slide, and, the clustering of the megaclasts. The

553   megaclast clusters then induced internal velocity perturbation that could result in the

554   initiation and cessation of intra-MTC flow cells.

555   6. *En masse* freezing was unlikely to occur throughout the body of the Gorgon Slide at the same

556   time. Instead, 'punctuated' freezing, where Cell A has halted while Cell B was still in motion,

557   occurred due to differential friction and pore-fluid pressure dissipation at flow cells margins.

558   For instance, excess pore-fluid can be maintained within the longitudinal shear zone, so that

559   Cell B only experienced minimal friction despite Cell A impeded its movement. In contrast,

560   excess pore-fluid pressure was likely to dissipate at lateral margins (e.g. the NE lateral margin

561   separating Cell A and stationary substrate). Thus, Cell A experienced higher lateral friction

562   than that of Cell B, resulting in reduced runout distance. This punctuated freezing mechanism

563   may be considered for modelling the impact of MTCs on submarine infrastructures.

569   **CONFLICT OF INTEREST**

570 No conflict of interest declared.

REFERENCES

572 ALSOP, G.I., AND MARCO, S., 2011, Soft-sediment deformation within seismogenic slumps of the Dead

573   Sea Basin: Journal of Structural Geology, v. 33, p. 433-457.

574 ALSOP, G.I., AND MARCO, S., 2014, Fold and fabric relationships in temporally and spatially evolving

575   slump systems: A multi-cell flow model: Journal of Structural Geology, v. 63, p. 27-49.

576 ALVES, T.M., KURTEV, K., MOORE, G.F., AND STRASSER, M., 2014, Assessing the internal character, reservoir

577   potential, and seal competence of mass-transport deposits using seismic texture: A

578   geophysical and petrophysical approach: AAPG Bulletin, v. 98, p. 793-824.

579 ALVES, T.M., 2015, Submarine slide blocks and associated soft-sediment deformation in deep-water

580   basins: A review: Marine and Petroleum Geology, v. 67, p. 262-285.

581 APTHORPE, M., 1988, Cainozoic depositional history of the North West Shelf: The North West Shelf,

582   Australia: Petroleum Exploration Society of Australia, p. 55-84.

583 BOYD, R., WILLIAMSON, P., AND HAQ, B., 1993, Seismic Stratigraphy and Passive-Margin Evolution of the

584   Southern Exmouth Plateau, *in* Posamentier, H.W., Summerhayes, C.P., Haq, B.U., and Allen,

585   G.P., eds., Sequence Stratigraphy and Facies Associations: Oxford, Blackwell Scientific

586   Publications, p. 579-603.

587 BROWN, A.R., 2011, Interpretation of three-dimensional seismic data: AAPG Memoir 42, SEG

588   Investigations in Geophysics No. 9: Tulsa, The American Association of Petroleum Geologists

589   and the Society of Exploration Geophysicists.

590 BULL, S., CARTWRIGHT, J., AND HUUSE, M., 2009, A review of kinematic indicators from mass-transport

591   complexes using 3D seismic data: Marine and Petroleum Geology, v. 26, p. 1132-1151.

592 BULL, S., AND CARTWRIGHT, J.A., 2019, Line length balancing to evaluate multi-phase submarine landslide

593   development: an example from the Storegga Slide, Norway: Geological Society, London,

594   Special Publications, v. 500.

595 BUTLER, R., AND MCCAFFREY, W., 2010, Structural evolution and sediment entrainment in mass-transport

596   complexes: outcrop studies from Italy: Journal of the Geological Society, v. 167, p. 617-631.

597   CARDONA, S., WOOD, L.J., DUGAN, B., JOBE, Z., AND STRACHAN, L.J., 2020, Characterization of the Rapanui

598   mass-transport deposit and the basal shear zone: Mount Messenger Formation, Taranaki

599   Basin, New Zealand: Sedimentology.

600   CATHRO, D.L., AUSTIN JR, J.A., AND MOSS, G.D., 2003, Progradation along a deeply submerged

601   OligoceneMiocene heterozoan carbonate shelf: How sensitive are clinoforms to sea level

602   variations?: AAPG bulletin, v. 87, p. 1547-1574.

603   CHOPRA, S., AND MARFURT, K.J., 2007, Seismic attributes for prospect identification and reservoir

604   characterization, v. 11, Society of Exploration Geophysicists Tulsa, Oklahoma.

605   CLEGG, L., SAYERS, M., AND TAIT, A., 1992, The Gorgon Gas Field: Chapter 32.

606   DE HAAS, T., BRAAT, L., LEUVEN, J.R., LOKHORST, I.R., AND KLEINHANS, M.G., 2015, Effects of debris flow

607   composition on runout, depositional mechanisms, and deposit morphology in laboratory

608   experiments: Journal of Geophysical Research: Earth Surface, v. 120, p. 1949-1972.

609   DOTT, R., 1963, Dynamics of subaqueous gravity depositional processes: AAPG Bulletin, v. 47, p. 104-

610   128.

611   DYKSTRA, M., GARYFALOU, K., KERTZNUS, V., KNELLER, B., MILANA, J.P., MOLINARO, M., SZUMAN, M., AND

612   THOMPSON, P., 2011, Mass-transport deposits: Combining outcrop studies and seismic forward

613   modeling to understand lithofacies distributions, deformations, and their seismic stratigraphic

614   expression: SEPM Special Publication, v. 96, p. 293-310.

615   ECKERSLEY, A.J., LOWELL, J., AND SZAFIAN, P., 2018, High-definition frequency decomposition: Geophysical

616   Prospecting, v. 66, p. 1138-1143.

617   FARRELL, S.G., 1984, A dislocation model applied to slump structures, Ainsa Basin, South Central

618   Pyrenees: Journal of Structural Geology, v. 6, p. 727-736.

619   FISHER, R.V., 1983, Flow transformations in sediment gravity flows: Geology, v. 11, p. 273-274.

620   FLEMING, R.W., AND JOHNSON, A.M., 1989, Structures associated with strike-slip faults that bound

621   landslide elements: Engineering Geology, v. 27, p. 39-114.

622   FOSSEN, H., 2016, Structural geology, Cambridge University Press.

623　FREY-MARTINEZ, J., CARTWRIGHT, J., AND HALL, B., 2005, 3D seismic interpretation of slump complexes:

624　　　examples from the continental margin of Israel: Basin Research, v. 17, p. 83-108.

625　FREY-MARTÍNEZ, J., CARTWRIGHT, J., AND JAMES, D., 2006, Frontally confined versus frontally emergent

626　　　submarine landslides: A 3D seismic characterisation: Marine and Petroleum Geology, v. 23, p.

627　　　585-604.

628　GAMBOA, D., ALVES, T., CARTWRIGHT, J., AND TERRINHA, P., 2010, MTD distribution on a 'passive' continental

629　　　margin: The Espírito Santo Basin (SE Brazil) during the Palaeogene: Marine and Petroleum

630　　　Geology, v. 27, p. 1311-1324.

631　GAMBOA, D., AND ALVES, T.M., 2015, Three-dimensional fault meshes and multi-layer shear in mass-

632　　　transport blocks: Implications for fluid flow on continental margins: Tectonophysics, v. 647, p.

633　　　21-32.

634　GEE, M., MASSON, D., WATTS, A., AND ALLEN, P., 1999, The Saharan debris flow: an insight into the

635　　　mechanics of long runout submarine debris flows: Sedimentology, v. 46, p. 317-335.

636　GEE, M., GAWTHORPE, R., AND FRIEDMANN, J., 2005, Giant striations at the base of a submarine landslide:

637　　　Marine Geology, v. 214, p. 287-294.

638　GEE, M., GAWTHORPE, R., AND FRIEDMANN, S., 2006, Triggering and evolution of a giant submarine

639　　　landslide, offshore Angola, revealed by 3D seismic stratigraphy and geomorphology: Journal

640　　　of Sedimentary Research, v. 76, p. 9-19.

641　GEE, M.J., MASSON, D.G., WATTS, A.B., AND MITCHELL, N.C., 2001, Passage of debris flows and turbidity

642　　　currents through a topographic constriction: seafloor erosion and deflection of flow

643　　　pathways: Sedimentology, v. 48, p. 1389-1409.

644　GOLOVCHENKO, X., BORELLA, P.E., AND O'CONNELL, S.B., 1992, Sedimentary cycles on the Exmouth Plateau,

645　　　*in* Von Rad, U., Haq, B.U., Kidd, R.B., and O'Connell, S.B., eds., Proceedings of the Ocean Drilling

646　　　Program, Scientific Results: College Station, TX, Ocean Drilling Program, p. 279-291.

647   HENGESH, J.V., DIRSTEIN, J.K., AND STANLEY, A.J., 2013, Landslide geomorphology along the Exmouth

648   Plateau continental margin, North West Shelf, Australia: Australian Geomechanics, v. 48, p.

649   71-92.

650   HODGSON, D., BROOKS, H., ORTIZ-KARPF, A., SPYCHALA, Y., LEE, D., AND JACKSON, C.-L., 2018, Entrainment and

651   abrasion of megaclasts during submarine landsliding and their impact on flow behaviour:

652   Geological Society, London, Special Publications, v. 477, p. SP477. 26.

653   HULL, J.N.F., AND GRIFFITHS, C.M., 2002, Sequence stratigraphic evolution of the Albian to Recent section

654   of the Dampier Sub-basin, NorthWest Shelf, Australia: The Sedimentary Basins of Western

655   Australia 3: Proceedings of the Petroleum Exploration Society of Australia Symposium, p. 617-

656   639.

657   IVERSON, R.M., 1997, The physics of debris flows: Reviews of geophysics, v. 35, p. 245-296.

658   JACKSON, C.A., 2011, Three-dimensional seismic analysis of megaclast deformation within a mass

659   transport deposit; implications for debris flow kinematics: Geology, v. 39, p. 203-206.

660   JOANNE, C., LAMARCHE, G., AND COLLOT, J.Y., 2013, Dynamics of giant mass transport in deep submarine

661   environments: the Matakaoa Debris Flow, New Zealand: Basin Research, v. 25, p. 471-488.

662   KEEP, M., POWELL, C., AND BAILLIE, P., 1998, Neogene deformation of the North West Shelf, Australia: The

663   sedimentary basins of Western Australia, v. 2, p. 81-91.

664   LASTRAS, G., DE BLASIO, F.V., CANALS, M., AND ELVERHØI, A., 2005, Conceptual and numerical modeling of

665   the BIG'95 debris flow, western Mediterranean Sea: Journal of Sedimentary Research, v. 75,

666   p. 784-797.

667   LONGLEY, I.M., BUESSENSCHUETT, C., CLYDSDALE, L., CUBITT, C.J., DAVIS, R.C., JOHNSON, M.K., MARSHALL, N.M.,

668   MURRAY, A.P., SOMERVILLE, R., AND SPRY, T.B., 2002, The North West Shelf of Australia - a

669   Woodside Perspective, *in* Keep, M., and Moss, S.J., eds., The Sedimentary Basins of Western

670   Australia 3: Petroleum Exploration Society of Australia Symposium: Perth, p. 28-88.

671   LUCENTE, C.C., AND PINI, G.A., 2003, Anatomy and emplacement mechanism of a large submarine slide

672   within a Miocene foredeep in the northern Apennines, Italy: A field perspective: American

673   Journal of Science, v. 303, p. 565-602.

674   MAJOR, J.J., AND IVERSON, R.M., 1999, Debris-flow deposition: Effects of pore-fluid pressure and friction

675   concentrated at flow margins: Geological Society of America Bulletin, v. 111, p. 1424-1434.

676   MARTINSEN, O., 1994, Mass movements, The geological deformation of sediments, Springer, p. 127-

677   165.

678   MASSON, D., HUGGETT, Q., AND BRUNSDEN, D., 1993, The surface texture of the Saharan debris flow

679   deposit and some speculations on submarine debris flow processes: Sedimentology, v. 40, p.

680   583-598.

681   MASSON, D., HARBITZ, C., WYNN, R., PEDERSEN, G., AND LØVHOLT, F., 2006, Submarine landslides: processes,

682   triggers and hazard prediction: Philosophical Transactions of the Royal Society A:

683   Mathematical, Physical and Engineering Sciences, v. 364, p. 2009-2039.

684   MAZZANTI, P., AND DE BLASIO, F., 2010, Peculiar morphologies of subaqueous landslide deposits and their

685   relationship to flow dynamics, Submarine mass movements and their consequences, Springer,

686   p. 141-151.

687   MCARDELL, B.W., BARTELT, P., AND KOWALSKI, J., 2007, Field observations of basal forces and fluid pore

688   pressure in a debris flow: Geophysical research letters, v. 34.

689   MCCORMACK, K., AND MCCLAY, K., 2013, Structural Architecture of the Gorgon Platform, North West

690   Shelf, Australia: The Sedimentary Basins of Western Australia IV: Proceedings of the

691   Petroleum Exploration Society of Australia Symposium, Perth, WA, p. 24.

692   MCGILVERY, T.A.H., GEOFFREY, 2004, Seafloor and shallow subsurface examples of mass transport

693   complexes, Offshore Brunei, Offshore Technology Conference: Houston.

694   MOHRIG, D., ELLIS, C., PARKER, G., WHIPPLE, K.X., AND HONDZO, M., 1998, Hydroplaning of subaqueous

695   debris flows: Geological Society of America Bulletin, v. 110, p. 387-394.

696   MOSCARDELLI, L., AND WOOD, L., 2008, New classification system for mass transport complexes in
697   offshore Trinidad: Basin Research, v. 20, p. 73-98.

698   MOSS, G.D., CATHRO, D.L., AND AUSTIN, J.A., 2004, Sequence biostratigraphy of prograding clinoforms,
699   northern Carnarvon Basin, Western Australia: a proxy for variations in Oligocene to Pliocene
700   global sea level?: Palaios, v. 19, p. 206-226.

701   NARDIN, T.R., HEIN, F., GORSLINE, D.S., AND EDWARDS, B., 1979, A review of mass movement processes
702   sediment and acoustic characteristics, and contrasts in slope and base-of-slope systems versus
703   canyon-fan-basin floor systems.

704   NEMEC, W., 1991, Aspects of sediment movement on steep delta slopes, *in* Colella, A., and Prior, D.B.,
705   eds., Coarsed-Grained Deltas, International Association of Sedimentologists, p. 29-73.

706   NUGRAHA, H.D., JACKSON, C.A.-L., JOHNSON, H.D., HODGSON, D.M., AND CLARE, M., 2019a, How erosive are
707   submarine landslides?, EarthArXiv.

708   NUGRAHA, H.D., JACKSON, C.A., JOHNSON, H.D., HODGSON, D.M., AND REEVE, M.T., 2019b, Tectonic and
709   oceanographic process interactions archived in Late Cretaceous to Present deep-marine
710   stratigraphy on the Exmouth Plateau, offshore NW Australia: Basin Research, v. 31, p. 405-
711   430.

712   OGATA, K., MOUNTJOY, J., PINI, G.A., FESTA, A., AND TINTERRI, R., 2014, Shear zone liquefaction in mass
713   transport deposit emplacement: a multi-scale integration of seismic reflection and outcrop
714   data: Marine Geology, v. 356, p. 50-64.

715   OMERU, T., AND CARTWRIGHT, J.A., 2019, The efficacy of kinematic indicators in a complexly deformed
716   Mass Transport Deposit: Insights from the deepwater Taranaki Basin, New Zealand: Marine
717   and Petroleum Geology, v. 106, p. 74-87.

718   ORTIZ-KARPF, A., HODGSON, D.M., JACKSON, C.A.-L., AND McCAFFREY, W.D., 2017, Influence of Seabed
719   Morphology and Substrate Composition On Mass-Transport Flow Processes and Pathways:
720   Insights From the Magdalena Fan, Offshore Colombia: Journal of Sedimentary Research, v. 87,
721   p. 189-209.

722   PARKER, E.J., TRAVERSO, C.M., MOORE, R., EVANS, T., AND USHER, N., 2008, Evaluation of landslide impact
723   on deepwater submarine pipelines: Offshore technology conference.

724   PARTYKA, G., GRIDLEY, J., AND LOPEZ, J., 1999, Interpretational applications of spectral decomposition in
725   reservoir characterization: The Leading Edge, v. 18, p. 353-360.

726   POSAMENTIER, H.W., AND KOLLA, V., 2003, Seismic geomorphology and stratigraphy of depositional
727   elements in deep-water settings: Journal of Sedimentary Research, v. 73, p. 367-388.

728   POSAMENTIER, H.W., AND MARTINSEN, O.J., 2011, The character and genesis of submarine mass-transport
729   deposits: insights from outcrop and 3D seismic data: Mass-transport deposits in deepwater
730   settings: Society for Sedimentary Geology (SEPM) Special Publication 96, p. 7-38.

731   PRÉLAT, A., PANKHANIA, S.S., JACKSON, C.A.-L., AND HODGSON, D.M., 2015, Slope gradient and lithology as
732   controls on the initiation of submarine slope gullies; Insights from the North Carnarvon Basin,
733   Offshore NW Australia: Sedimentary Geology, v. 329, p. 12-17.

734   PRIOR, D.B., BORNHOLD, B., AND JOHNS, M., 1984, Depositional characteristics of a submarine debris flow:
735   The Journal of Geology, v. 92, p. 707-727.

736   RANDOLPH, M.F., AND WHITE, D.J., 2012, Interaction forces between pipelines and submarine slides—A
737   geotechnical viewpoint: Ocean Engineering, v. 48, p. 32-37.

738   SAWYER, D.E., FLEMINGS, P.B., DUGAN, B., AND GERMAINE, J.T., 2009, Retrogressive failures recorded in
739   mass transport deposits in the Ursa Basin, Northern Gulf of Mexico: Journal of Geophysical
740   Research: Solid Earth, v. 114.

741   SCARSELLI, N., MCCLAY, K., AND ELDERS, C., 2013, Submarine slide and slump complexes, Exmouth Plateau,
742   NW Shelf of Australia: The Sedimentary Basins of Western Australia IV: Proceedings of the
743   Petroleum Exploration Society of Australia Symposium.

744   SOBIESIAK, M.S., KNELLER, B., ALSOP, G.I., AND MILANA, J.P., 2018, Styles of basal interaction beneath mass
745   transport deposits: Marine and Petroleum Geology, v. 98, p. 629-639.

746   SOBIESIAK, M.S., BUSO, V.V., KNELLER, B., ALSOP, G.I., AND MILANA, J.P., 2019, Block Generation,
747   Deformation, and Interaction of Mass-Transport Deposits With the Seafloor: An Outcrop-

748   Based Study of the Carboniferous Paganzo Basin (Cerro Bola, NW Argentina): Submarine

749   Landslides: Subaqueous Mass Transport Deposits from Outcrops to Seismic Profiles, p. 91-104.

750   STEVENTON, M.J., JACKSON, C.A., HODGSON, D.M., AND JOHNSON, H.D., 2019, Strain analysis of a seismically

751   imaged mass-transport complex, offshore Uruguay: Basin Research, v. 31, p. 600-620.

752   SUN, Q., ALVES, T., LU, X., CHEN, C., AND XIE, X., 2018, True volumes of slope failure estimated from a

753   Quartenary mass-transport deposit in the northern South China Sea: Geophysical Research

754   Letters.

755   TALLING, P.J., MASSON, D.G., SUMNER, E.J., AND MALGESINI, G., 2012, Subaqueous sediment density flows:

756   Depositional processes and deposit types: Sedimentology, v. 59, p. 1937-2003.

757   TINDALE, K., NEWELL, N., KEALL, J., AND SMITH, N., 1998, Structural evolution and charge history of the

758   Exmouth Sub-basin, Northern Carnarvon Basin, Western Australia, *in* Purcell, P.G., and Purcell,

759   R.R., eds., The Sedimentary Basins of Western Australia 2: Proceedings of the Petroleum

760   Exploration Society of Australia: Perth, p. 473-490.

761   TRINCARDI, F., AND ARGNANI, A., 1990, Gela submarine slide: a major basin-wide event in the Plio-

762   Quaternary foredeep of Sicily: Geo-Marine Letters, v. 10, p. 13.

763   VANNESTE, M., FORSBERG, C.F., GLIMSDAL, S., HARBITZ, C.B., ISSLER, D., KVALSTAD, T.J., LØVHOLT, F., AND NADIM,

764   F., 2013, Submarine landslides and their consequences: what do we know, what can we do?,

765   Landslide science and practice, Springer, p. 5-17.

766   VARNES, D.J., 1978, Slope movement types and processes: Special report, v. 176, p. 11-33.

767   WEIMER, P., AND SHIPP, C., 2004, Mass Transport Complexes: Musing on past uses and suggestions for

768   future directions, Offshore Technology Conference: Houston.

769   ZAKERI, A., 2009, Review of state-of-the-art: Drag forces on submarine pipelines and piles caused by

770   landslide or debris flow impact: Journal of offshore mechanics and Arctic engineering, v. 131.

771   ZENG, H., HENRY, S.C., AND RIOLA, J.P., 1998, Stratal slicing, Part II: Real 3-D seismic data: Geophysics, v.

772   63, p. 514-522.

773   **FIGURE CAPTIONS**

774   **Fig. 1.--- A)** Location of the study area. Regional seismic line (orange) across several wells (see Fig. 2).

775   **B)** Seabed map of the Gorgon Slide, and industry well data (red dots) available for this study. The

776   Gorgon Slide is expressed as rugose relief on the seabed. Both evacuation and most of deposition

777   zones are imaged within the 3D seismic reflection data. **C)** Outline of the deposits of the Gorgon Slide

778   (dark grey), where a minor area (c. 7%) of the total slide area in the NW (dashed line) is not imaged

779   within the 3D seismic reflection data. This minor part is delineated using 2D seismic lines (green). Five

780   3D seismic reflection datasets (Gorgon, Acme, Draeck, Duyfken, and Io-Jansz) were used in this study.

781   Bathymetry and topography data are from Geoscience Australia.

782   **Fig. 2.---** A regional seismic section across the Exmouth Plateau (see Fig. 1 for location). **A)**

783   Uninterpreted. **B)** Interpreted. The Gorgon Slide is bound by a basal-shear surface (yellow) at the base

784   and seabed (blue) at the top. Modified from Nugraha et al. (2019b).

785   **Fig. 3.--- A)** Thickness map of the Gorgon Slide showing lateral boundaries of the slide (i.e. NE lateral

786   margin and pinch-out in the SW), with thickness concentration adjacent to the NE lateral margin. We

787   divide rugged geometry of the frontal margin into eastern and western frontal margins. **B)** Seabed dip

788   map showing two distinct sub-bodies (namely Area A and B) within the slide. The two areas are

789   separated by a zone of longitudinal shear. The depositional zone of the slide comprises upper (UTD)

790   and lower (LTD) translation and toe domains. **C)** A 3D perspective of seabed structure map in the LTD

791   showing the geometry of the longitudinal shear zone.

792   **Fig. 4.--- A)** Dip-oriented seismic section across the Gorgon Slide showing the headwall scarp,

793   evacuation and deposition zones. **B)** Strike-oriented seismic section showing the asymmetric

794   geometry of the slide, with erosional lateral margin in the NE and pinch-out in the SW.

795   **Fig. 5.---** Seismic facies classification used in this study. **A)** Seismic facies description and

796   interpretation. **B)** Variance attributes extraction between the basal-shear surface and an iso-

797   proportional surface (50% between the basal-shear surface and the seabed). **C-E)** Seismic sections

798   showing seismic facies within the translation domain. **F)** A time-slice of variance attribute extraction

799   (see G for position) showing seismic facies in the toe domain. **G)** A seismic section showing seismic

800   facies in the toe domain.

801   **Fig. 6.---** Seabed map showing kinematic indicators in the headwall domain, which include the main

802   headwall of the Gorgon Slide, grooves, crown cracks, pockmarks, and a small scarp. **A)** Uninterpreted.

803   **B)** Interpreted.

804   **Fig. 7.---** Upper translation domain of the Gorgon Slide. **A)** Basal-shear surface variance map (top) and

805   its interpretation (bottom). **B)** Internal body RMS amplitude map (extracted 50 ms above and below

806   isoproportional horizon, orange) (top) and its interpretation (bottom). **C)** Top surface dip map (top)

807   and its interpretation (bottom). **D)** Seismic sections, uninterpreted (above) and interpreted (bottom),

808   showing seismic facies across the upper translation domain. See text for discussions.

809   **Fig. 8.--- A)** Spectral decomposition map within the slide (50% between basal-shear and top surfaces)

810   showing features within upper translation domain in detail. **B)** Uninterpreted, and **C)** interpreted,

811   seismic section along megaclasts (SF-4) across Area A and B. See text for discussion.

812   **Fig. 9.---** Lower translation domain of the Gorgon Slide. **A)** Basal-shear surface variance map (top) and

813   its interpretation (bottom). **B)** Internal body RMS amplitude map (extracted 50 ms above and below

814   isoproportional horizon, orange) (top) and its interpretation (bottom). **C)** Top surface dip map (top)

815   and its interpretation (bottom). **D)** Seismic sections, uninterpreted (above) and interpreted (bottom),

816   showing seismic facies across the upper translation domain. See text for discussion.

817   **Fig. 10.---** Dimensions and orientation of the megaclasts in the upper and lower translation domains.

818   **A)** Megaclasts in the upper translation domain are generally thinner with longer long-axes, as

819   compared to the ones in the lower translation domain that are thicker with shorter long-axes. **B)**

820   Megaclasts in the upper translation domain are generally oriented perpendicular, and the ones in the

821   lower translation domain are oblique to sub-parallel, to the transport direction.

822   **Fig. 11.---** Toe domain of the Gorgon Slide. **A)** Basal-shear surface variance map (top) and its

823   interpretation (bottom). **B)** Internal body RMS amplitude map (time-slice at the orange horizon in D)

824   (top) and its interpretation (bottom). **C)** Top surface dip map (top) and its interpretation (bottom). **D)**

825   Seismic sections, uninterpreted (above) and interpreted (bottom), showing seismic facies across the
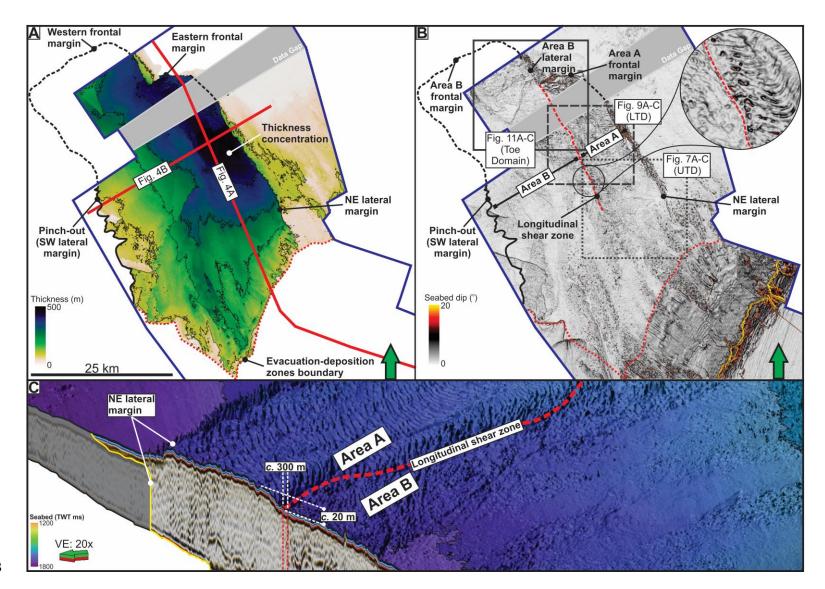
826   toe domain. See text for discussion.

827   **Fig. 12.---** Schematic diagram of Gorgon Slide depicting three stages of emplacement processes. **A)** A

828   failure event occurred. **B)** The slide split into two flow cells, Cell A and B, due to a cluster of megaclasts

829   derived from the headwall and/or slope strata that acted as a flow obstacle. **C)** Cell A ceased, and its

830   frontal margin is expressed on the seabed, while Cell B flowed beyond the limit of the dataset. See

831   text for discussion.

832   **Fig. 13.---** **A)** Variance map extracted along the orange horizon in C-D, overlaid by time structure map

833   of thrusted megaclasts (see the red horizon in D, left). The thrusted megaclasts define the frontal

834   margin of Cell A and lateral margin of Cell B. **B)** Variance map extracted along the basal-shear surface

835   (yellow) in C-D, overlaid by time structure map of the basal megaclasts (see the red horizon in D, right).

836   **C)** Uninterpreted, and **D)** interpreted seismic section across the thrusted and basal megaclasts. These

837   megaclasts have similar dimension and seismic facies, thus, likely to have a similar origin.

Figure 1

840   Figure 2

Exmouth Plateau Arch ━━━━━━━━━━━━━━━━━━━━━━━━━━ **Kangaroo Syncline** ━━ **NW Shelf**

A
NW
ODP 762   Scarborough 4A   Jupiter 1   Chandon 1   Jansz 3   Orthrus 1   Bluebell 1   SE

TWT (ms): 500, 1000, 1500, 2000, 2500, 3000, 3500, 4000

50 km

Study Area

B
ODP 762   Scarborough 4A   Jupiter 1   Chandon 1   Jansz 3   Orthrus 1   Bluebell 1

The Gorgon Slide

TWT (ms): 500, 1000, 1500, 2000, 2500, 3000, 3500, 4000

50 km

Triassic or older   Jurassic   Berriasian - Valanginian   Berremian - Aptian (Muderong Shale)   Albian - Cenomanian
Turonian - Maastrichtian   Palaeocene - L. Miocene   L. Miocene - Recent   **Basal-shear surface of the Gorgon Slide**   **Seabed**

841

842   Figure 3

843

Figure 4

Facies	Description	Interpretation
SF-1	Chaotic and transparent both in cross-section and map-view (Fig. 5B-C).	Debrites containing disaggregated materials (cf. Posamentier and Kolla 2003).
SF-2	Low-to-medium amplitude, discontinuous folded reflections that occasionally form sinuous lineations in map-view (Fig. 5B, D-E).	Debrites containing partially disaggregated materials (cf. Ortiz-Karpf et al. 2017).
SF-3	High amplitude, discontinuous folded reflections that are separated by imbricate thrusts (Fig. 5F-G).	Fold and thrust systems formed by compressional deformation within MTCs, flow direction is generally perpendicular to the strike of the thrusts (Bull et al. 2009).
SF-4	Isolated packages of coherent, sub-parallel reflections within a matrix composed of SF-1 or 2 (Fig. 5B-C, E). In most cases, the reflections are disrupted, e.g. faulted and folded.	Megaclasts transported within debritic matrix (cf. Bull et al. 2009; Jackson 2011; Hodgson et al. 2018).
SF-5	Medium-to-high amplitude, continuous, sub-parallel, downslope-dipping reflections beneath the shelf and within the evacuation zone (Fig. 4A).	Non-MTC deposits, i.e. carbonate progradation and layered slope deposits that were the source of, and eroded by, the Gorgon Slide (Hengesh et al. 2013; Nugraha et al. 2019b).

848   Figure 6

849

850   Figure 7

A Basal-shear surface (Variance) **B** Internal body (RMS Amplitude) **C** Top surface/seabed (Dip)

Map

Interpretation

Fig. 7D

Variance 1 / 0

5 km

RMS Amplitude 2500 / 0

Fig. 8

Dip 20 / 0

Older MTC

Deformed substrate

Shear fractures

Lateral margin

Ramp

Grooves

Internal shear zone

Convex-downslope shear bands

Convex-upslope shear bands

Longitudinal shear zone

Megaclast

Cluster of megaclasts

Transport direction

Convex-downslope ridges

Area A

Area B

Convex-upslope ridges

Internal shear zone

Lateral margin

Upslope limit of longitudinal shear zone

D SW   NE

100 ms

Folded reflection

Deformed substrate

Older MTC

Megaclast   Ramp   2.5 km

100 ms

2.5 km

Seismic facies within the Gorgon Slide   SF-1   SF-2   SF-3   SF-4

851

852   Figure 8

A
Internal shear zone within Area A
Convex-downslope shear bands
Lateral margin
Longitudinal shear zone
Convex-upslope shear bands
Fig. 8B-C
Megaclasts offset by the longitudinal shear zone
49 Hz
29 Hz   64 Hz
2 km

B NW
Megaclasts
Megaclasts
SE

C
2 km
100 ms

853

854   Figure 9

Seismic facies within the Gorgon Slide   SF-1   SF-2   SF-3   SF-4

855

856   Figure 10

857

A Basal-shear surface (Variance)   **B** Internal body (RMS Amplitude)   **C** Top surface/seabed (Dip)

Seismic facies within the Gorgon Slide   SF-1   SF-2   SF-3   SF-4

Figure 12

A
- Surface rupture
- Future evacuation-deposition zones boundary
- Pre-existing thrusted megaclasts encased within an Older MTC
- Pre-existing strata
- Approximate scale
- c. 40 km
- c. 500 m
- c. 15 km

B
- Megaclasts were clustered and become an obstacle to flow
- Initial formation point of the longitudinal shear zone
- Cell A and B started to form downslope from the cluster of megaclasts
- Cell A
- Cell B
- Downslope-converging grooves
- Ridges
- Basal-shear surface propagated downslope

C
- Cluster of megaclasts
- A shadow zone was formed and narrowed downslope from the cluster of megaclasts
- Cell B travelled faster than Cell A
- Groove
- Internal shear zone
- Cell A
- Cell B
- Ridges
- The pre-existing megaclasts forced downslope translation of Cell A to cease

862   Figure 13

863